Supporting Information

Multilayer Graphene Crystals with Enhanced Performances in Oxygen Reduction and Zinc-Air Batteries via Interlayer Carbon Promoted O=O Bond Dissociation

*Yongfang Qu,[†a,c] Qian Tang,[†b] Dandan Wang,[†a] Bing He,[*a] Yong Liu,[c] Wei Chen,[b] Guangtao Yu,[*b] Boyuan Tang,[d] Fujian Liu[*a] and Liangti Qu[*e]*

[a] School of Chemistry and Chemical Engineering, Shaoxing University, Shaoxing, 312000 China. E-mail: hebing@usx.edu.cn; fjliu@usx.edu.cn

[b] Engineering Research Center of Industrial Biocatalysis, Fujian Provincial Key Laboratory of Advanced Materials Oriented Chemical Engineering, Fujian-Taiwan Science and Technology Cooperation Base of Biomedical Materials and Tissue Engineering, College of Chemistry and Materials Science, Academy of Carbon Neutrality of Fujian Normal University, Fujian Normal University, Fuzhou 350007, China. E-mail: yugt@fjnu.edu.cn

[c] Henan Key Laboratory of Polyoxometalate Chemistry, College of Chemistry and Chemical Engineering, Henan University, Kaifeng, 475004, China.

[d] School of Material Science and Engineering, University of New South Wales, Sydney, New South Wales, 2052, Australia.

[e] Key Laboratory of Organic Optoelectronics & Molecular Engineering, Ministry of Education, Department of Chemistry, Tsinghua University, Beijing, 100084 China. E-mail: lqu@mail.tsinghua.edu.cn

† The authors contributed equally to this work.

Content

Supplementary Note

Experimental Section

Materials. Pyrrole was purchased from Shanghai Macklin Biochemical Co., ltd. Ferric trichloride and hydrochloric acid were purchased from Sinopharm Group Chemical Reagent Co. LTD. All of the chemicals were of analytic grade and used as received without further purification.

Synthesis of NM-MGCs. 1.0 mL of pyrrole was placed into the mortar, then, 3.0 g of ferric trichloride initiator was introduced with rapidly grounded until the formation of homogenous black polymer powder (NM-MGCs). The obtained black NM-MGCs powder was carbonized under nitrogen flow in a quartz crucible at 600 °C for 4 h, further heating to 800 °C within 2 h and maintained at 800 °C for another 1 h. Finally, the carbonized product was stirred into 3.0 M HCl solution at room temperature overnight and successively washed by using distilled water for two times to remove any residual Fe species, followed by a vacuum drying at 60 °C, giving the NM-MGC-800. The NM-MGC-700 and NM-MGC-900 were prepared with the same procedure as that of NM-MGC-800, except for the final carbonization temperature at 700 °C and 900 °C, respectively.

Synthesis of CP-2-800. CP-2-800 were synthesized from classical solvent polymerization of pyrrole tandem its carbonization route according to the previously reported method.[1]

Characterizations

X-ray diffraction (XRD) tests were recorded on an X'Pert3 Powder diffractometer using Cu Kα radiation (40 mA, 45 kV). Scanning electron microscopic (SEM) analysis was performed over an S-4800 Hitachi at an acceleration voltage of 5 kV. Transmission electron microscope (TEM) images were obtained on a Zeiss Libra200 TEM at an acceleration voltage of 200 kV. Specific surface areas and pore volumes were determined from adsorption−desorption isotherms of nitrogen at −196 °C using a Micromeritics ASAP 2020M system, the sample was degassed under vacuum (1×10^{-5} Pa) at 180 °C for 6 h prior to measurement. X-ray photoelectron spectroscopic (XPS) analysis was performed on a Thermo Fisher Scientific EscaLab 250Xi instrument. Laser Raman (Raman) spectra were collected on a Renishaw InVia Reflex spectrometer with laser wavelength of 532 nm and power of 100 mW. Contact angles were obtained using a contact angle measuring instrument (SC16000E). Atomic force microscopy (AFM) studies were conducted on a Nanoscope IVA electron microscope. The inductively coupled plasma mass spectrometer (ICP-MS, Optima 8000, PerkinElmer, USA) was used to analyze the metal content. The In situ attenuated total reflectance surface-enhanced infrared absorption spectroscopy (ATR-SEIRAS) was employed on a Nicolet 6700 spectrometer equipped with the MCT detector. The catalysts were loaded onto a silicon wafer working electrode coated with a thin layer of gold nanoparticles. The electrochemical tests were conducted in O_2-saturated 0.1 M KOH, adopting the saturated calomel electrode as RE. The O_2 adsorption isotherms were measured on a Micromeritics TriStar II 3020 analyzer. Typically, 100 mg sample was pretreated at 200 °C for 3 h to remove adsorbed water and impurities, and then the adsorbed amount of O_2 for the sample was measured at 25 °C. O_2-temperature programmed desorption mass spectrometry (O_2-TPD-MS) analyses were performed on a Micromeritics AutoChem II 2920 system equipped with HPR-20 R&D mass detector, the electric current

and voltage of the mass detector under working condition was 20 μA and 800 V, respectively. Individual m/z profiles were recorded over the mass of 16, 18, 28, 32, 44 amu, in which purified He was employed as the carrier gas. Typically, 100 mg of the sample was loaded in the quartz tube, and the sample was first purged with a He (20 mL min^{-1}) at 200 °C for 3 h before the measurement. After dropping to room temperature, the sample was purged with pure O_2 (30 mL min^{-1}) for 1 h, and then the sample was purged under He gas for 40 minutes to remove the physically adsorbed O_2. The temperature was then raised to 600 °C while the detector signals were recorded simultaneously.

Electrochemical measurement

The electrochemical measurements were carried out using a CHI 760D electrochemical workstation (Shanghai Chenhua Ltd., China) equipped with RRDE-3A Apparatus (ALS, Japan) using a typical three-electrode system, containing of saturated calomel electrode (SCE) reference electrode, Platinum wire counter electrode and modified glassy carbon working electrode. For preparation of the catalyst ink, dispersing 3.5 mg of samples in 500 μL mixture solvent of isopropanol (120 μL), deionized water (370 μL) and Nafion (10 μL) (5 wt.%, DuPont) with ultrasonicated for 30 min, 4 μL homogeneous suspension were deposited on 3 mm RDE achieving 0.4 mg cm^{-2} loadings as working electrode. The catalyst loading for commercial Pt/C (20 wt.%, JM) catalysts was also 0.4 mg cm^{-2}. All the measured potentials were converted to the reversible hydrogen electrode (RHE): $E_{RHE}=E_{SCE}+0.0591\times pH+0.241$.

The cyclic voltammetry (CV) and linear sweep voltammetry (LSV) tests were performed at a scan rate of 50 and 10 mV s^{-1}, respectively. The current-time (i-t) curves were collected at 0.8 V (*vs.* RHE). The ring electrode voltage was 1.51 V (*vs.* RHE) using RRDE electrode as working electrode. The H_2O_2 yield and electron transfer number *n* were obtained using the following equations:

$$n = \frac{4I_D}{I_D + (I_R / N)} \tag{1}$$

$$\%H_2O_2 = 100 \times \frac{2I_R / N}{I_D + (I_R / N)} \tag{2}$$

The I_D and I_R is the disk current and ring current, and N = 0.424 is the collection efficiency of the Pt ring.

RDE tests were performed with rotating speed of 400-2500 rpm. The electron transfer number (*n*) can be obtained by the Koutecky-Levich equation:

$$\frac{1}{J} = \frac{1}{J_K} + \frac{1}{J_L} = \frac{1}{J_K} + \frac{1}{B\omega^{1/2}} \tag{3}$$

$$B0.62nFC_O(D_O)^{2/3}\upsilon^{-1/6} = \tag{4}$$

$$J_K = nFkC_O \tag{5}$$

In which J, J_k, and J_L represent the measured, kinetic-limited, and diffusion-limited current densities, respectively, ω represents electrode rotation rate, n is the number of electrons transferred per oxygen molecule, F is the Faraday constant (96500 C mol^{-1}), C_O is the concentration of O_2 (1.2×10^{-3} M), D_O

represents diffusion coefficient of O_2 (1.9×10^{-5} cm^2 s^{-1}), υ presents solution stickiness (0.01 cm^2 s^{-1}), and k is electron-transfer rate constant.

Assembly and testing of zinc-air batteries (ZABs)

The liquid-state Zn-air batteries were evaluated in a homemade electrochemical cell, utilizing a polished Zn plate (0.2 mm thickness) as the anode and a catalyst-loaded paper (loading of 2.0 mg cm^{-2}) as the cathode at room temperature. The employed electrolyte was a mixed aqueous solution of KOH (6 M) and $Zn(OAc)_2$ (0.2 M). The cathode of the Zn-air battery was made as follows: A composite substrate material with a thickness of ~ 610 μM was fabricated by integrating nickel foam, waterproof film, and carbon paper. The catalyst ink was prepared by ultrasonic dispersion of 10 mg of the samples or 20 wt.% Pt/C in 1 mL of (960 μL anhydrous ethanol + 40 μL Nafion) solution. Then, 2 mg of the catalyst ink was deposited on the composite substrate within an area of 1 cm^2 as the cathode. The specific capacity was calculated according to the following equation 6:

$$\text{Specific capacity (mA h g}^{-1}) = I \times t/\omega_{Zn} \quad (6)$$

where I, t and ω_{Zn} represent the applied current, cycle time and the weight of zinc consumed, respectively. The polarization test was conducted using an electrochemical workstation CHI 760D, and the galvanostatic discharge and discharge–charge cycle tests were conducted using the LAND CT3002A test system.

The flexible solid-state Zn-air battery was obtained using a polished zinc foil (0.10 mm thickness) as anode, the carbon cloth (1×2 cm^2) loading of catalyst as air electrode with a Ni foam as current collector, and the gel polymer as solid electrolyte. The gel polymer electrolyte was prepared as follows: 1.0 g poly(vinyl alcohol) (PVA) powder (MW 19500, Aladdin) was dissolved in 10.0 mL deionized water at 95 °C under magnetic stirring for 2.0 h. Then 1.0 mL of 6 M KOH filled with 0.2 M $Zn(OAc)_2$ was added and the electrolyte solution was continuing stirred for 30 min at 95 °C. Then the solution was frozen at -3 °C over 12 h, and then thawed at room temperature to obtain the solid electrolyte.

Density functional theory calculations

Computational methods

All density function theory (DFT) calculations are performed using the Vienna *ab initio* simulation package (VASP).[2] The exchange correlation is described by the Perdew–Burke–Ernzerhof (PBE)[3] functional under the generalized gradient approximation (GGA),[4] incorporating the van der Waals interactions through the Grimme DFT-D2 approach.[5] The projected augmented wave (PAW)[6] pseudopotential is used to manipulate the electron-ion interactions. A 400-eV energy cutoff is employed to truncate the plane wave basis. For all geometric relaxations, $3 \times 3 \times 1$ Monkhorst-pack k-points are utilized in the first Brillouin zone, and the convergence thresholds are set at 10^{-4} eV for energy and 0.05 $eVÅ^{-1}$ for atomic force. A vacuum space of 20 Å in the z direction is created to eliminate potential interactions between adjacent periodic images.

Theoretical models

Based on our relevant experimental results, we initially construct a 10×10 supercell of N-doped single-layered graphene with a hole of appropriate size, where three representative modes of N-doping are considered, namely graphitic-N, pyridinic-N and pyrrolic-N, as illustrated in Fig. S13a. Subsequently, we have constructed the double-layered theoretical model based on this single-layered graphene, adopting the AB stacking similar to the graphitic case (Fig. S13b). This model is used to simulate the ORR system achieved experimentally in our study. In this theoretical model, the calculated lattice parameters are a=24.35 Å and b=24.33 Å, and the calculated C-C and C-N bond lengths are in the range of 1.38~1.49 and 1.33~1.45 Å, respectively. Additionally, the calculated interlayer distance is about 3.16 Å, and the diameter of hole is around 11.60 Å, both of which can closely match the corresponding experimental results. Furthermore, the interaction energy has been assessed using the formula $E_{int} = E_{double\text{-}layer} - 2 \times E_{single\text{-}layer}$. Our computed E_{int} value can be as large as -7.02 eV, indicating high structural stability, which can also be well consistent with the related experimental findings.

The free-energy calculations on oxygen reduction reaction (ORR)

The ORR process is the four-electron (4*e*) pathway for the conversion of oxygen to water. It usually involves two main 4*e* reduction pathways, namely, the oxygen dissociation and association pathways, as shown in the following:

Dissociation pathway:

$$O_2^* \rightarrow O^* + O^*$$

$$O^* + O^* + H_2O + e^- \rightarrow O^* + OH^* + OH^-$$

$$O^* + OH^* + e^- \rightarrow O^* + OH^-$$

$$O^* + H_2O + e^- \rightarrow OH^* + OH^-$$

$$OH^* + H_2O + e^- \rightarrow H_2O^* + OH^-$$

Association pathway:

$$O_2^* + H_2O + e^- \rightarrow OOH^* + OH^-$$

$$OOH^* + e^- \rightarrow O^* + OH^-$$

$$O^* + H_2O + e^- \rightarrow OH^* + OH^-$$

$$OH^* + H_2O + e^- \rightarrow H_2O^* + OH^-$$

These electrochemical free energy pathways are constructed from the DFT-calculated free energies (ΔG) using the computational model proposed by Nørskov.[7,8] The ΔG value in each elementary step of ORR is defined as:

$$\Delta G = \Delta E + \Delta E_{ZPE} - T\Delta S + \Delta G_U + \Delta G_{pH}$$

where ΔE, ΔE_{ZPE} and ΔS are the difference of total energy, zero point energy and entropy before and after the reaction, respectively. The temperature T is 298.15 K, and $\Delta G_U = -neU$, in which U is the electrode potential. $\Delta G_{pH} = k_B T \ln 10 \times pH$ is the correction for Gibbs free energy depending on concentration of H^+ ion,

in which k_B is Boltzmann's constant. In this work, pH = 13 is chosen to reflect an alkaline environment based on the experimental conditions. The overpotential (η) of the oxygen reduction reaction on the catalytic surface can be calculated by the formula $\eta = \eta_{eq} - \eta_{applied}$. Moreover, the side reaction producing H_2O_2 through the two-electron (2e) step is considered to evaluate the selectivity of the catalyst.

In the cathodic ORR reaction, oxygen adsorption initiates the process, and play a crucial role in determining the overall reaction pathways. In this work, three presentative oxygen adsorption configurations on the theoretical model are considered, that is, two O atoms in the O_2 molecule interacting simultaneously with two C atoms, each situated in different graphene layers adjacent to graphitic-N, pyridinic-N, or pyrrolic-N, as depicted in Fig. S14. Specifically, the O_2 adsorption energy (ΔE_{O2}) is calculated using the formula $\Delta E_{O2} = E_{slab\text{-}O2} - E_{slab} - E_{O2}$, where $\Delta E_{slab\text{-}O2}$, ΔE_{slab}, and ΔE_{O2} represent the total energies of the adsorbed O_2 on the slab, the isolated slab and the O_2 molecule, respectively. As shown in Fig. S14, the calculated adsorption energy ΔE_{O2} on the C atoms (0.05 eV) neighboring to graphitic-N can be significantly more favorable compared to those associated with pyridinic-N (2.69 eV) or pyrrolic-N (1.58 eV). This indicates that the relevant C atoms adjacent to the graphitic-N can be considered as the optimal site for O_2 adsorption. Especially, the corresponding O_2 adsorption energy ΔE_{O2} (0.05 eV) can even be close to zero, indicating an appropriate adsorption state of O_2 on the studied system, which will facilitate the subsequent ORR reaction process. Consequently, this study will primarily focus on the adsorption of O_2 on the relevant C atoms adjacent to the graphitic-N.

1. Supporting Figures

Fig. S1 Scale-up synthesis graph of NM-MGCs catalyst.

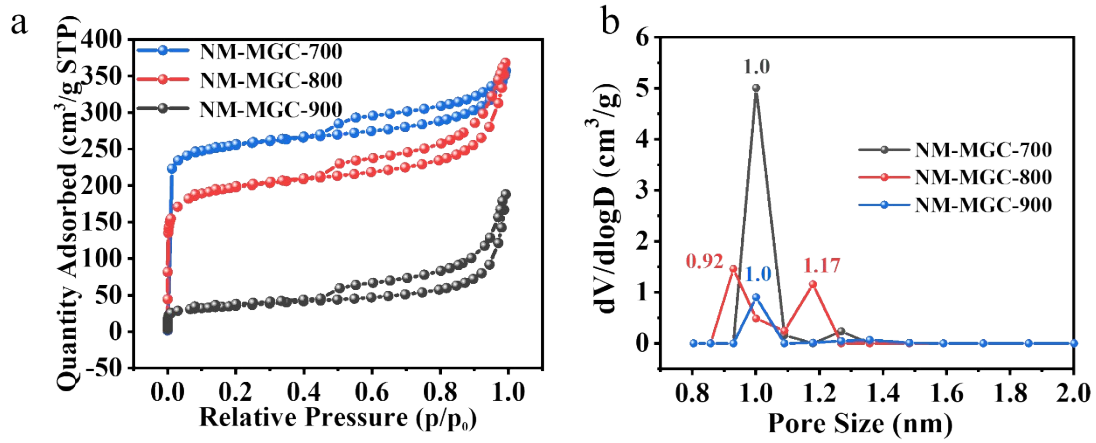

Fig. S2 (a) N_2 sorption isotherms and (b) pore size distribution curves of various NM-MGC samples.

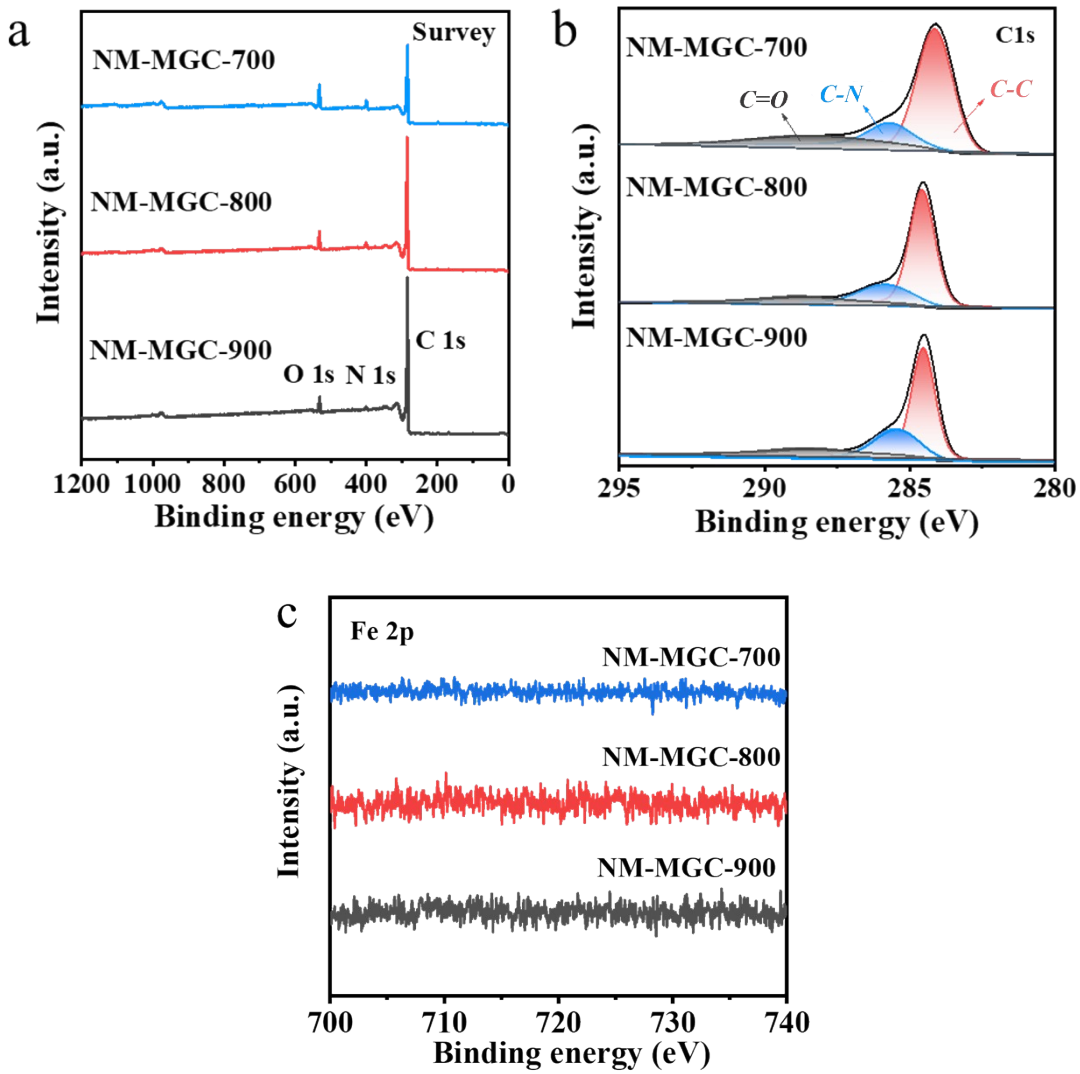

Fig. S3 (a) XPS survey spectrum, (b, c) high-resolution C1s and Fe 2p spectrum of NM-MGC.

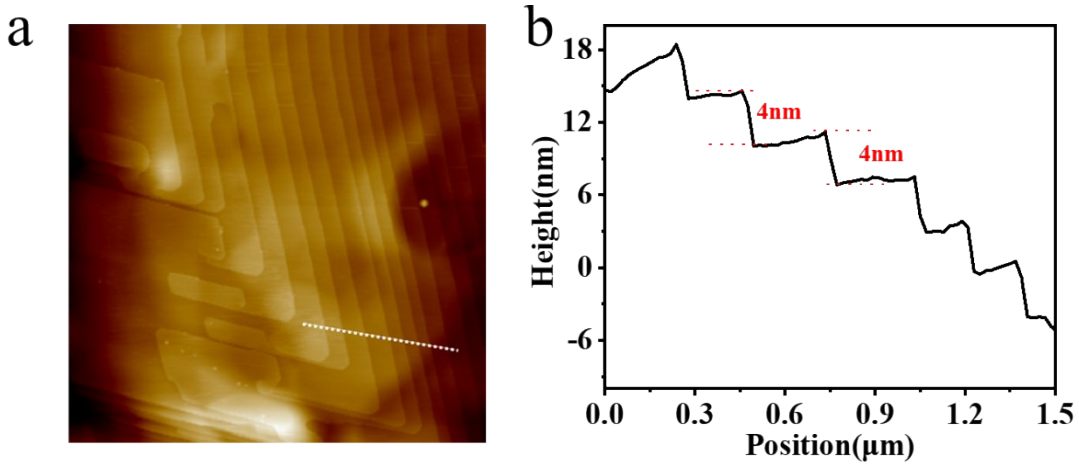

Fig. S4 (a) AFM image and (b) the corresponding height profiles of NM-MGC-800.

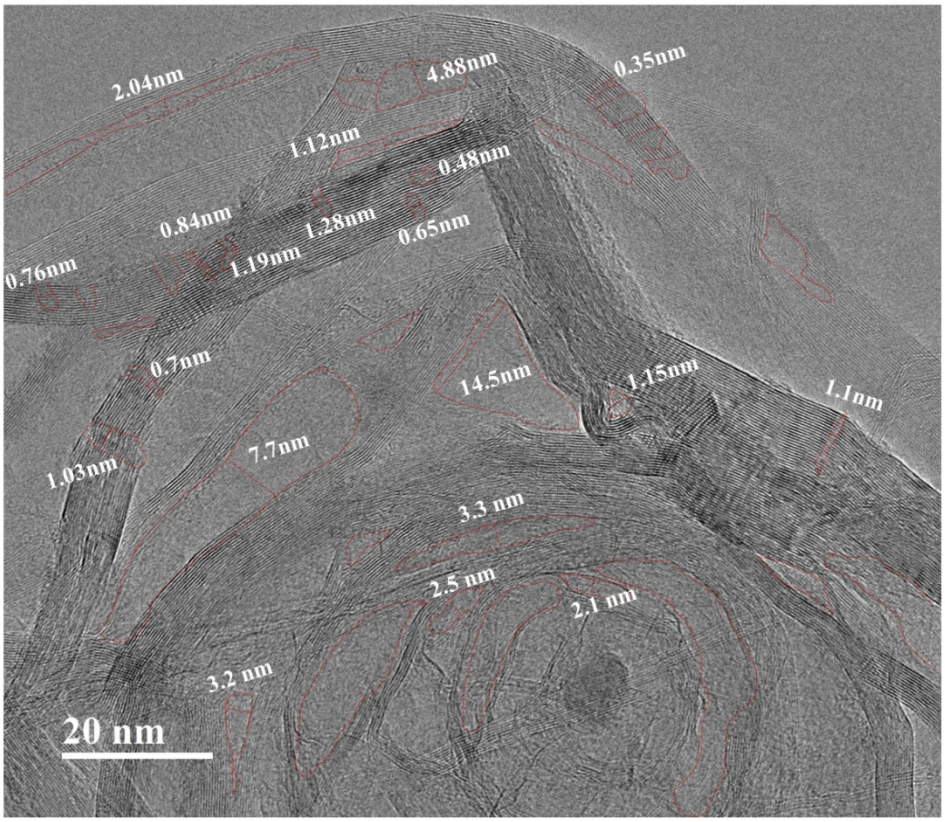

Fig. S5 HRTEM image of NM-MGC-800.

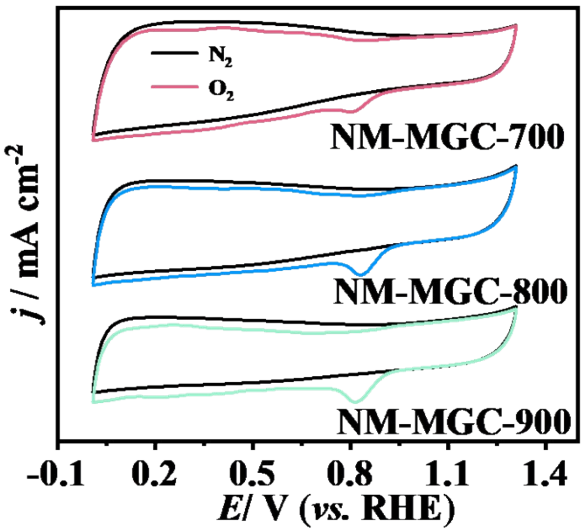

Fig. S6 CV curves of NM-MGCs in N_2- and O_2-saturated 0.1 M KOH.

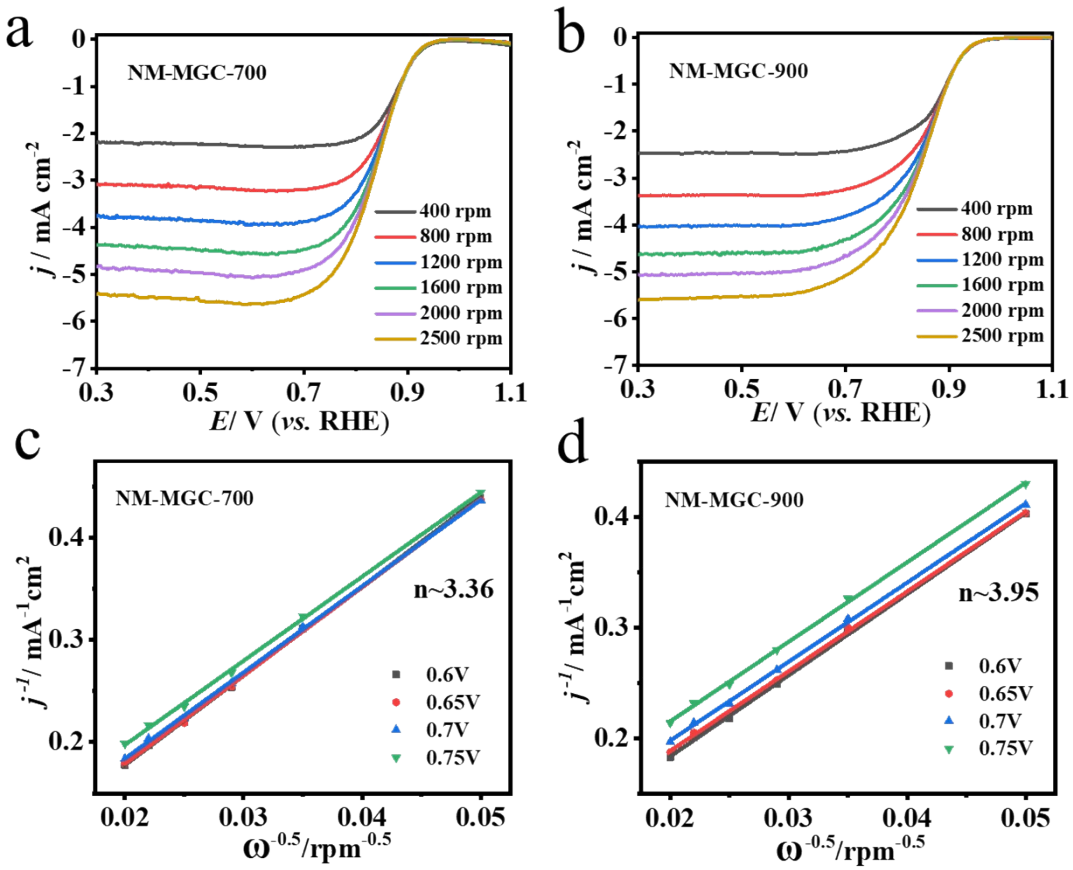

Fig. S7 (a, b) LSV curves in O_2-saturated 0.1 M KOH at different rotational speeds and (c, d) the related K-L plots (0.6-0.75 V) of NM-MGC-700 and NM-MGC-900.

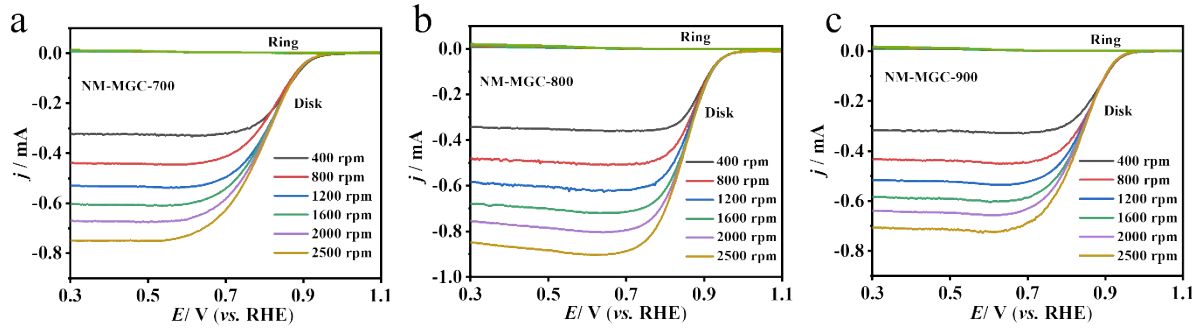

Fig. S8 (a, b, c) Ring and Disk current measured by RRDE of NM-MGCs.

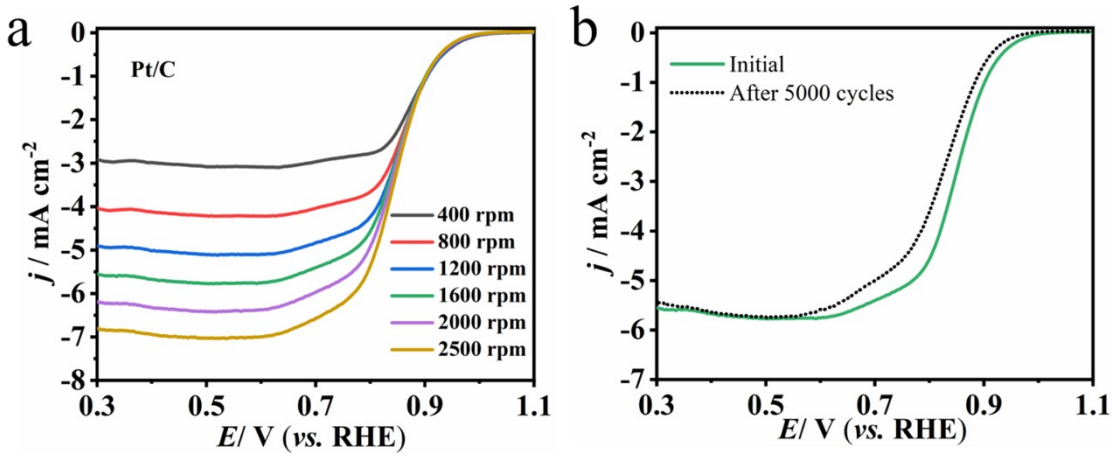

Fig. S9 (a) LSV curves for Pt/C in O_2-saturated 0.1 M KOH at different rotational speeds, (b) LSV results for Pt/C before and after the durability experiment for 5000 CV cycles in 0.1 M KOH.

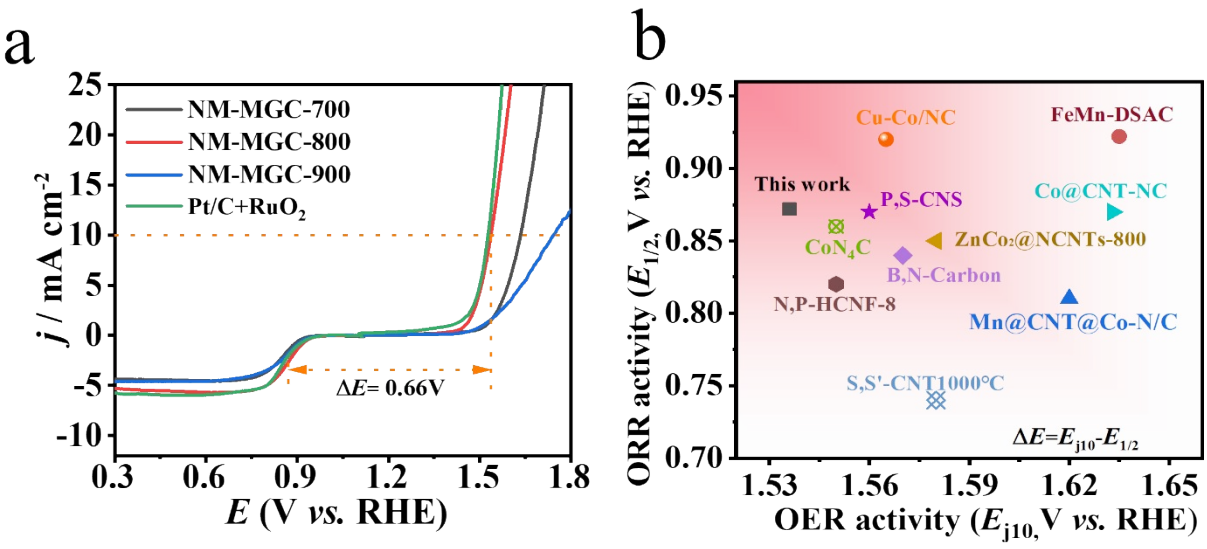

Fig. S10 (a) LSV polarization curves for ORR and OER activity; (b) Comparison of the E_{gap} values of NM-MGC-800 with various reported samples in the literatures.

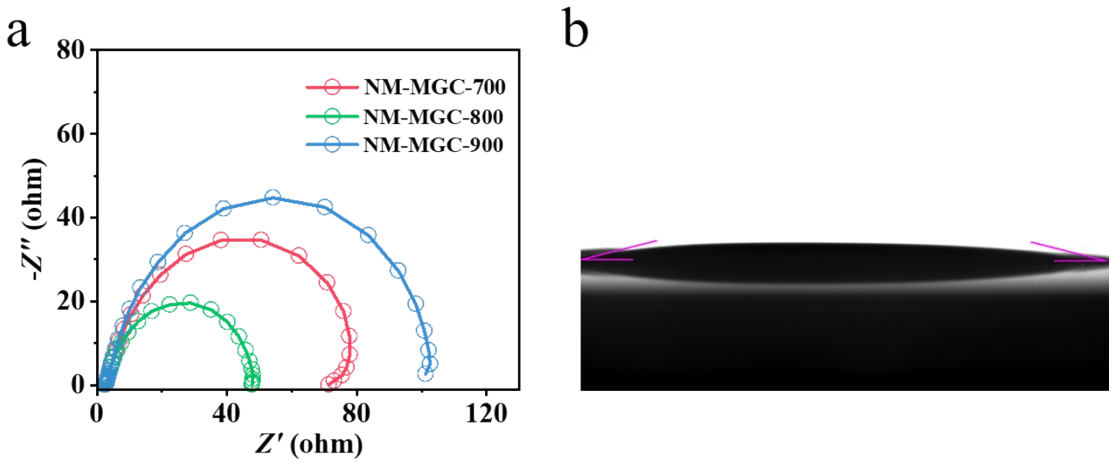

Fig. S11 (a) EIS plots of NM-MGCs; (b) Contact angle of NM-MGC-800 for the ZABs electrolyte.

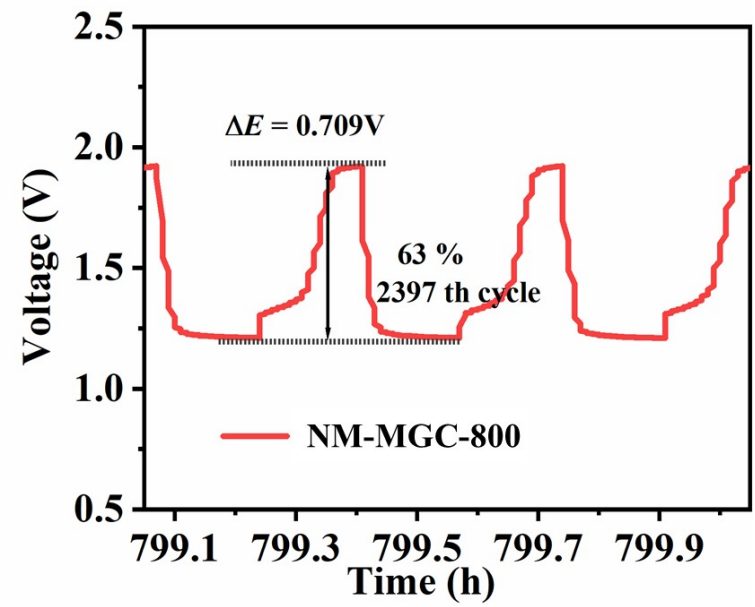

Fig. S12 Discharge charge cycling curves profile of NM-MGC-800.

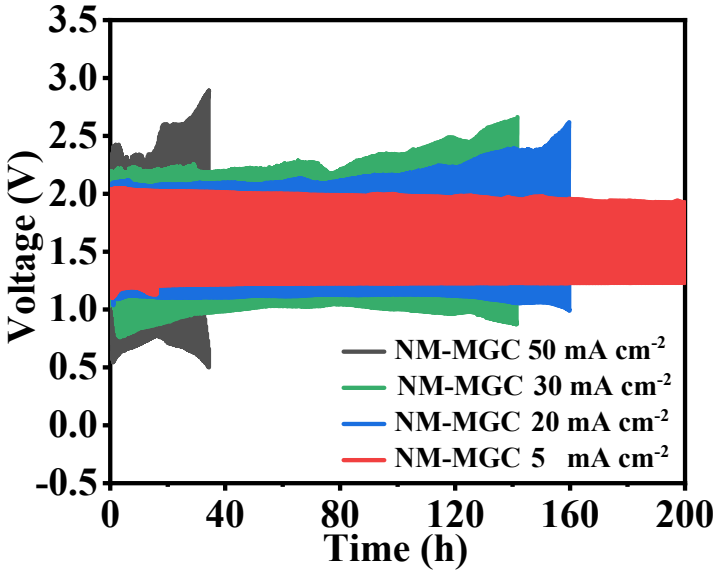

Fig. S13 Discharge charge cycling curves of NM-MGC-800 at different current density.

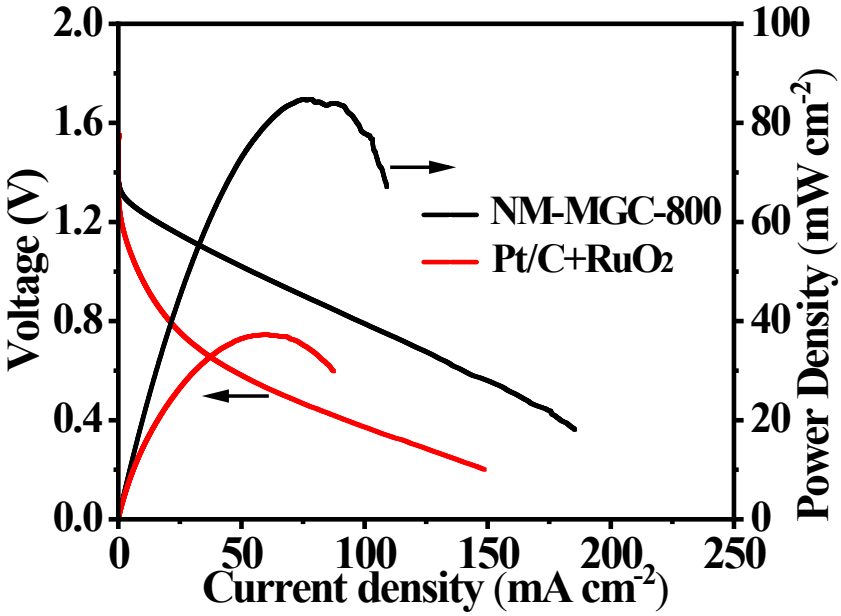

Fig. S14 Power density curves of NM-MGC-800 and Pt/C+RuO_2-based quasi-solid-state flexible ZABs.

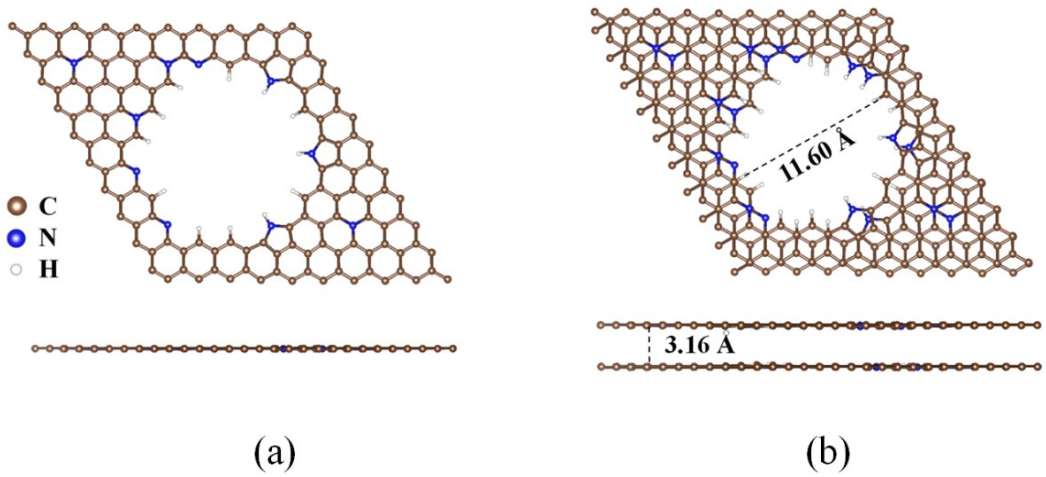

Fig. S15 The theoretical models of single-layer (a) and double-layer (b) N-doped graphene systems with a hole of appropriate size.

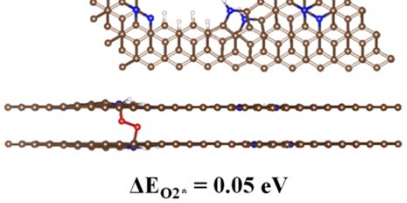

ΔE_{O2^*} = 0.05 eV

(b)

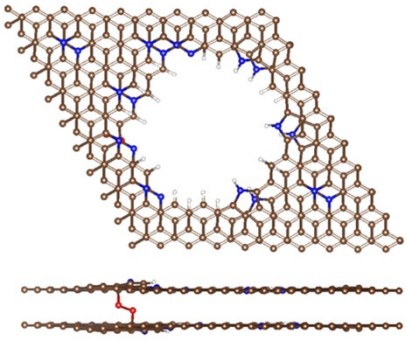

ΔE_{O2^*} = 2.69 eV

(c)

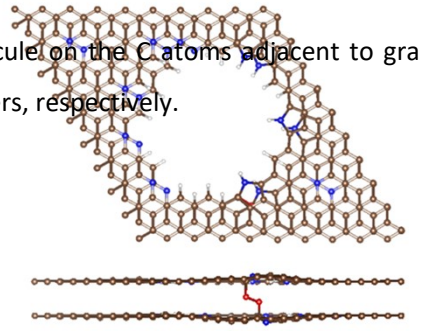

ΔE_{O2^*} = 1.58 eV

Fig. S16 The adsorption of O_2 molecule on the C atoms adjacent to graphitic-N (a), pyridinic-N (b) and pyrrolic-N (c) located in different layers, respectively.

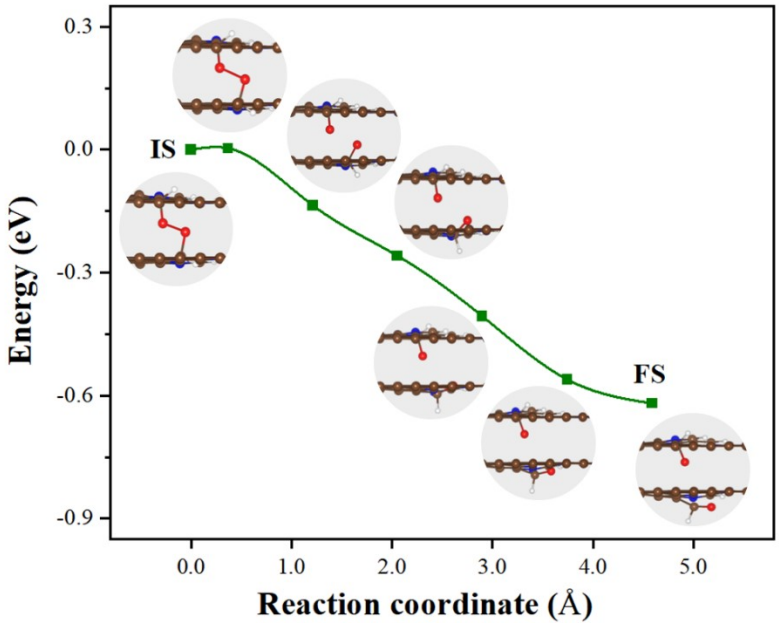

Fig. S17 The reaction pathway of O_2 dissociation on the catalyst, where O_2 adsorption configuration is set to zero. IS and FS represent the initial state and final state, respectively.

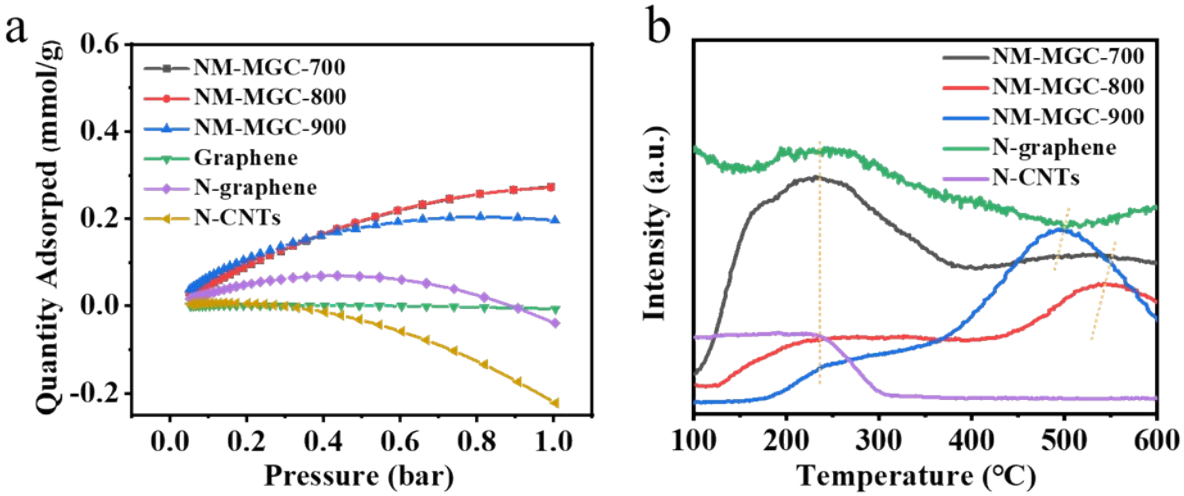

Fig. S18 (a) O_2 adsorption isotherms and O_2-TPD-MS profiles of NM-MGCs-x, Graphene, N-graphene and N-CNTs.

Table S1. The yields of the obtained NM-MGCs-800 and literature-reported porous carbon materials.

Sample	Raw material	HCl and water treatment	Yield	References
NM-MGC-800	1.0 g Py	0.641 g	64.1%	This work
CP-2-800	1.0 g Py	0.227 g	22.7%	Adv. Funct. Mater. 2011, 21, 2781–2787
Fe/N/C-SiO_2-HT1	0.2 g Fe/Phen/C	0.117 g	58.5%	Electrochimica Acta 2017, 244, 47–53
Fe/N/C-SiO_2-HT2	0.2 g Fe/Phen/C	0.079 g	39.7%	
Fe/N/C-HT1	0.2 g Fe/Phen/C	0.126 g	6.3%	
ZIF-67-NaCl-800	/	/	38.5%	Matter 2022, 5, 1603–1615
Glucose-NaCl-800	/	/	26.6%	
PVDF-NaCl-800	/	/	33.0%	
Leaf-NaCl-800	/	/	37.3%	

Table S2. Textural parameters of the obtained NM-MGCs-x samples.

Sample	S_{BET} [a] (m^2/g)	V_p [b] (cm^3/g)	Micro/meso/macropore volume percentage [c]
NM-MGC-700	811	0.31	69.2%/22.9%/7.9%
NM-MGC-800	624	0.22	64.6%/23.9%/11.5%
NM-MGC-900	117	0.02	13.6%/46.7%/39.7%

[a] BET surface area;

[b] V_p calculated by the t-plot method;

[c] Micropore volume was calculated by the DFT method; mesopore and macropore volumes were calculated by the BJH model. Micropore: 0−2.0 nm, mesopore: 2.0−50.0 nm, and macropore: >50 nm.

Table S3. Composition of the NM-MGCs.

Samples	Atomic ratio (%) [a]			Ratio of N sites (%)				Mass ratio (%)[b]
	C	N	O	pyridine-N	pyrrole- N	graphitic-N	oxidized-N	Fe
NM-MGC-700	82.70	9.64	7.66	31	30	16	23	~0
NM-MGC-800	91.61	5.59	2.79	22	25	38	15	~0
NM-MGC-900	93.02	4.64	2.34	18	24	39	19	~0

[a] Estimated from XPS results

[b] Estimated from ICP-OES results

Table S4. Comparison of $E_{1/2}$ and E_{j10} in alkaline media of NM-MGC-800 and previously reported ORR electrocatalysts.

Catalysts	$E_{1/2}$ (V vs. RHE)	E_{j10} (V vs. RHE)	References
NM-MGC-800	**0.872**	**1.536**	**This work**
FeMn-DSAC	0.922	1.635	9
Mn@CNT@Co-N/C	0.81	1.62	10
$ZnCo_2$@NCNTs-80	0.85	1.58	11
Co@CNT-NC	0.87	1.63	12
N,P-HCNF-8	0.82	1.55	13
Cu-Co/NC	0.92	1.565	14
S,S'-CNT1000℃	0.74	1.58	15
B,N-Carbon	0.84	11057	16
CoN_4C	0.86	1.55	17
P,S-CNS	0.87	1.56	18

Table S5. Comparison of $E_{1/2}$ and E_{onset} in alkaline media of NM-MGC-800 and previously reported ORR electrocatalysts.

Catalysts	$E_{1/2}$ (V vs. RHE)	E_{onset} (V vs. RHE)	References
NM-MGC-800	**0.872**	**0.996**	**This work**
B,N-Carbon	0.84	0.98	16
P,S-CNS	0.87	0.97	18
NPCNF-O	0.85	0.98	19
VP/CNs	0.86	1.08	20
BN-C-1	0.812	0.876	21
NCN-1000-5	0.82	0.95	22
NCR-1000	0.826	0.981	23
NDC1000	0.86	0.96	24
meso/micro-PoPD	0.87	0.98	25
PTA-1000	0.78	0.96	26
NCMT-1000	0.86	1.03	27
VA-NCNT/GC	0.865	0.965	28
ZrN	0.8	0.95	29
Co_3N/C	0.862	0.95	30
N-GRW	0.84	0.92	31

CoNC SAC	0.86	0.93	32
Zn/CoN-C	0.861	1.004	33
Co-pyridinic N-C	0.87	0.99	34
Co_{SA}/N,S-HCS	0.85	0.96	35
NCF	0.85	1	36

Table S6. Summary of performance based on NM-MGC-800 and recently reported state-of-the-art air-electrode based ZABs with alkaline electrolyte.

Catalysts	Peak power density (mW cm^{-2})	Specific capacity [mAh/g_{zn}@mA cm^{-2}]	Stability (h)	Ref.
NM-MGC-800	**221**	**854.3@5**	**800**	**This work**
P,S-CNS	198	830@5	100	18
CuS/NiS_2	172.4	775@5	83	37
P-$MnCo_2O_4$@PWC	160	811.3@10	400	38
$Fe_{SA/AC}$@HNC	171.5	811.8@20	130	39
Co_3S_4/FeS@CoFe/NC	170	816.3@1	680	40
Cu_3P/CoP@NC	209	765.6@10	317	41
PCN-226(Co)	133	724@20	Over160	42
Ru-SAS/SNC	229	728@10	270	43
FeMn-N-C	151	795	700	44
C-MOF-C_2-900	105	741@10	120	45
Fe/N-CNRs	181.8	771.7@10	100	46
$Fe_{0.5}$Co@HOMNCP	134	786.5@10	120	47
Fe_2O_3@NPCA	130	767@5	160	48
FeMn-DSAC	184	734@2	80	9

N-HPCs	158	829@5	100	49
Fe_2-pPc	255	791@10	450	50
$FeMn_{ac}$/Mn-N_4C	207	720.2	100	51

References

1 M. Sevilla, P. Valle-Vigóna and A. B. Fuertes, *Adv. Funct. Mater.* 2011, **21,** 2781–2787.

2 L. Zong, M. Li, P. Li, K. Fan and L. Wang, *Angew. Chem. Int. Ed.* 2024, e202413933.

3 G. Kresse and D. Joubert, *Phys. Rev. B* 1999, **59**, 1758–1775.

4 J. P. Perdew, K. Burke and M. Ernzerhof, *Phys. Rev. Lett.* 1996, **77**, 3865–3868.

5 S. Grimme, *J. Comput. Chem.* 2004, **25**, 1463–1473.

6 P. E. Blochl, *Phys. Rev. B* 1994, **50**, 17953–17979.

7 Q. Zhao, Z. Cao, X. Wang, H. Chen, Y. Shi, Z. Cheng, Y. Guo, B. Li, Y. Gong, Z. Du and S. Yang, *J. Am. Chem. Soc.* 2023, **145**, 21242–21252.

8 J. K. Norskov, J. Rossmeisl, A. Logadottir, L. Lindqvist, J. R. Kitchin, T. Bligaard and H. Jónsson, *J. Phys. Chem. B* 2004, **108**, 17886–17892.

9 T. T. Cui, Y. P. Wang, T. Ye, J. Wu, Z. Q. Chen, J. Li, Y. P. Lei, D. S. Wang and Y. D. Li, *Angew. Chem. Int. Ed.* 2022, **61**, e202115219.

10 F. Li, T. T. Qin, Y. P. Sun, R. J. Jiang, J. F. Yuan and X. Q. Liu, A. P. O'Mullane, *J. Mater. Chem. A* 2021, **9**, 22533–22543.

11 T. T. Qin, F. Li, X. Q. Liu, J. F. Yuan, R. J. Jiang, Y. P. Sun, H. J. Zheng and A. P. O'Mullane, *Chem. Eng. J.* 2022, **429**, 132199.

12 B. F. Gao, M. Y. Tan, W. H. Xi, X. F. Lin, Z. N. Li, M. R. Shen and B. Z. Lin, *J. Power Sources* 2022, **527**, 231205.

13 Y. Gao, Z. C. Xiao, D. B. Kong, R. Iqbal, Q. H. Yang and L. J. Zhi, *Nano Energy* 2019, **64**, 103879.

14 Z. J. Li, S. Q. Ji, C. Wang, H. X. Liu, L. P. Leng, L. Du, J. C. Gao, M. Qiao, J. H. Horton and Y. Wang, *Adv. Mater.* 2023, **35**, 2300905.

15 A. M. El-Sawy, I. M. Mosa, D. Su, C. J. Guild, S. Khalid, R. Joesten, J. F. Rusling and S. L. Suib, *Adv. Energy Mater.* 2016, **6**, 1501966.

16 T. Sun, J. Wang, C. T. Qiu, X. Ling, B. B. Tian, W. Chen and C. L. Su, *Adv. Sci.* 2018, **5**, 1800036.

17 J. Rong, E. R. Gao, N. C. Liu, W. Y. Chen, X. S. Rong, Y. Z. Zhang, X. D. Zheng, H. S. Ao, S. L. Xue, B. Huang, Z. Y. Li, F. X. Qiu and Y. T. Qian, *Energy Storage Mater.* 2023, **56**, 165–173.

18 S. S. Shinde, C.-H. Lee, A. Sami, D.-H. Kim, S.-U. Lee and J.-H. Lee, *ACS Nano* 2017, **11**, 347–357.

19 F. Qiang, J. Feng, H. Wang, J. Yu, J. Shi, M. Huang, Z. Shi, S. Liu, P. Li and L. Dong, *ACS Catal.* 2022, **12**, 4002–4015.

20 H. Xia, R. Pang, X. Dong, Q. Liu, J. Chen, E. Wang and J. Li, *J. Am. Chem. Soc.* 2023, **145**, 25695–25704.

21 M. Fan, Q. Yuan, Y. Zhao, Z. Wang, A. Wang, Y. Liu, K. Sun, J. Wu, L. Wang and J. Jiang, *Adv. Mater.* 2022, **34**, 2107040.

22 H. Jiang, J. Gu, X. Zheng, M. Liu, X. Qiu, L. Wang, W. Li, Z. Chen, X. Ji and J. Li, *Energy Environ. Sci.* 2019, **12**, 322–333.

23 Q. Lai, H. Zheng, Z. Tang, D. Bi, N. Chen, X. Liu, J. Zheng and Y. Liang, *ACS Appl. Mater. Interfaces* 2021, **13**, 61129–61138.

24 Q. Lai, J. Zheng, Z. Tang, D. Bi, J. Zhao and Y. Liang, *Angew. Chem. Int. Ed.* 2020, **59**, 11999–12006.

25 H.-W. Liang, X. Zhuang, S. Bruller, X. Feng and K. Mullen, *Nat. Commun.* 2014, **5**, 4973.

26 J. Wang, Y. Yao, C. Zhang, Q. Sun, D. Cheng, X. Huang, J. Feng, J. Wan, J. Zou, C. Liu and C. Yu, *Adv. Sci.* 2021, **8**, 2100120.

27 J.-C. Li, P.-X. Hou, S.-Y. Zhao, C. Liu, D.-M. Tang, M. Cheng, F. Zhang and H.-M. Cheng, *Energy Environ. Sci.* 2016, **9**, 3079–3084.

28 K. Gong, F. Du, Z. Xia, M. Durstock and L. Dai, *Science* 2009, **323**, 760–764.

29 Y. Yuan, J. Wang, S. Adimi, H. Shen, T. Thomas, R. Ma, J. P. Attfield and M. Yang, *Nat. Mater.* 2020, **19**, 282–286.

30 R. Zeng, Y. Yang, X. Feng, H. Li, L. M. Gibbs, F. J. DiSalvo and H. D. Abruna, *Sci. Adv.* 2022, **8**, eabj1584.

31 H. B. Yang, J. Miao, S.-F. Hung, J. Chen, H. B. Tao, X. Wang, L. Zhang, R. Chen, J. Gao, H. M. Chen, L. Dai and B. Liu, *Sci. Adv.* 2016, **2**, e1501122.

32 C.-X. Zhao, J.-N. Liu, J. Wang, C. Wang, X. Guo, X.-Y. Li, X. Chen, L. Song, B.-Q. Li and Q. Zhang, *Sci. Adv.* 2022, 8, eabn5091.

33 Z. Lu, B. Wang, Y. Hu, W. Liu, Y. Zhao, R. Yang, Z. Li, J. Luo, B. Chi, Z. Jiang, M. Li, S. Mu, S. Liao, J. Zhang and X. Sun, *Angew. Chem. Int. Ed.* 2019, **58**, 2622–2626.

34 Y. Ha, B. Fei, X. Yan, H. Xu, Z. Chen, L. Shi, M. Fu, W. Xu and R. Wu, *Adv. Energy Mater.* 2020, **10**, 2002592.

35 Z. Zhang, X. Zhao, S. Xi, L. Zhang, Z. Chen, Z. Zeng, M. Huang, H. Yang, B. Liu, S. J. Pennycook and P. Chen, *Adv. Energy Mater.* 2020, **10**, 2002896.

36 L. Zhang, T. Gu, K. Lu, L. Zhou, D.-S. Li and R. Wang, *Adv. Funct. Mater.* 2021, **31**, 2103187.

37 L. An, Y. Li, M. Luo, J. Yin, Y.-Q. Zhao, C. Xu, F. Cheng, Y. Yang, P. Xi and S. Guo, *Adv. Funct. Mater.* 2017, **27**, 1703779.

38 Y. Liu, S. Liu, P. Zhang, J. Zhou, H. Liu, S. Li, X. Li, X. Wang, D. Han, Y. Chen, Y. Wang, J. Jiang and B. Li, *Adv. Funct. Mater.* 2024, **34**, 2400522.

39 H. Zhang, H.-C. Chen, S. Feizpoor, L. Li, X. Zhang, X. Xu, Z. Zhuang, Z. Li, W. Hu, R. Snyders, D. Wang and C. Wang, *Adv. Mater.* 2024, **36**, 2400523.

40 Y. Tan, Y. Wang, A. Li, X. Jiang, Y. Zhang and C. Cheng, *Journal of Energy Chemistry* 2024, **96**, 568–577.

41 M. Guo, L. Wang, Z. Huang, H. Li, T. T. Isimjan and X. Yang, *ACS Nano* 2024, **18**, 17901–17912.

42 M. O. Cichocka, Z. Liang, D. Feng, S. Back, S. Siahrostami, X. Wang, L. Samperisi, Y. Sun, H. Xu, N. Hedin, H. Zheng, X. Zou, H.-C. Zhou and Z. Huang, *J. Am. Chem. Soc.* 2020, **142**, 15386–15395.

43 J. Qin, H. Liu, P. Zou, R. Zhang, C. Wang and H. L. Xin, *J. Am. Chem. Soc.* 2022, **144**, 2197–2207.

44 C. Hu, G. Xing, W. Han, Y. Hao, C. Zhang, Y. Zhang, C.-H. Kuo, H.-Y. Chen, F. Hu, L. Li and S. Peng, *Adv. Mater.* 2024, **36**, 2405763.

45 M. Zhang, Q. Dai, H. Zheng, M. Chen and L. Dai, *Adv. Mater.* 2018, **30**, 1705431.

46 X. Gong, J. Zhu, J. Li, R. Gao, Q. Zhou, Z. Zhang, H. Dou, L. Zhao, X. Sui, J. Cai, Y. Zhang, B. Liu, Y. Hu, A. Yu, S.-H. Sun, Z. Wang and Z. Chen, *Adv. Funct. Mater.* 2021, **31**, 2008085.

47 W. Li, B. Liu, D. Liu, P. Guo, J. Liu, R. Wang, Y. Guo, X. Tu, H. Pan, D. Sun, F. Fang and R. Wu, *Adv. Mater.* 2022, **34**, 2109605.

48 K. Wu, L. Zhang, Y. Yuan, L. Zhong, Z. Chen, X. Chi, H. Lu, Z. Chen, R. Zou, T. Li, C. Jiang, Y. Chen, X. Peng and J. Lu, *Adv. Mater.* 2020, **32**, 2002292.

49 F. Kong, X. Cui, Y. Huang, H. Yao, Y. Chen, H. Tian, G. Meng, C. Chen, Z. Chang and J. Shi, *Angew. Chem. Int. Ed.* 2022, **61**, e202116290.

50 Z. Huang, M. Li, X. Yang, T. Zhang, X. Wang, W. Song, J. Zhang, H. Wang, Y. Chen, J. Ding and W. Hu, *J. Am. Chem. Soc.* 2024, **146**, 24842–24854.

51 H. Liu, L. Jiang, J. Khan, X. Wang, J. Xiao, H. Zhang, H. Xie, L. Li, S. Wang and L. Han, *Angew. Chem. Int. Ed.* 2023, **62**, e202214988.